# High-Power Emission via Large-Area VCSELs With Single High-Order Mode Operation

Valerio Torrelli ⬤, Alberto Gullino ⬤, *Member, IEEE*, Alberto Tibaldi ⬤, *Member, IEEE*, Francesco Bertazzi ⬤, Michele Goano ⬤, *Senior Member, IEEE*, and Pierluigi Debernardi ⬤

*Abstract*—In this work we investigate patterned large-active area AlGaAs vertical-cavity surface-emitting lasers (VCSELs) targeting high-power single-transverse-mode emission. As a first step, our in-house 3D electromagnetic vectorial mode solver VELMS is validated against preliminary experimental data. Then, VELMS is applied to implement single-mode operation on VCSELs featuring large-area rectangular oxide apertures. A comparative appraisal of different mode selection strategies based on patterning the out-coupling facet of the device is presented, providing a number of alternatives for a broad audience of technologists.

*Index Terms*—VCSELs, High-Power, Large Active Area, Single-Mode Emission, Optical Mode Solvers.

## I. INTRODUCTION

VERTICAL-CAVITY surface-emitting lasers (VCSELs) are the reference light sources for a large number of commercial usages due to their compactness, single longitudinal mode, low power consumption and array-oriented manufacturing. Applications range from high-speed short-range data communication in data centers [1], to gas sensing [2], up to LiDAR for the automotive market [3].

In recent years, VCSELs are also being used as optical-pumping sources for atomic devices such as Cs-based atomic clocks, sensors, magnetometers and quantum gyroscopes [4], [5], [6], [7], [8], [9], [10], [11], [12]. The laser source in these devices is needed to populate the excited atomic states, therefore the VCSEL is required to feature a transverse single-mode emission at a specific target frequency, set at 795 nm in the case of rubidium atoms [5], [6], [13], [14], for which the standard AlGaAs-based technology, customary for data-center 850 nm VCSELs, is applicable.

The easiest way to achieve single mode emission is to exploit a small oxide aperture ($<3\,\mu$m). However, this strongly limits the output power and worsens the thermal roll-over due to the increased series resistance. As stated in [6], several designs have been proposed to increase the output power whilst remaining within the single-mode regime, such as surface-relief based circular VCSELs [15], [16] or circular devices whose epi-structure features a particular alignment between the oxide and the standing wave, obtained by modifying few p-DBR pairs [6]. Both solutions present a single mode power around $4 \div 6$ mW. However, these power levels are still quite low with respect to what can be achieved with VCSEL arrays or large active-area devices, featuring multi-mode emission, hence lower spectral purity. For instance, a VCSEL with a rectangular active area of dimensions $40 \times 10\,\mu$m$^2$ reported a multi-mode power of the order of tens of mW [17], [18].

Following the preliminary ideas expressed in [19], this work aims at investigating and designing large-area single-mode rectangular VCSELs. This is done by selecting a specific mode with different surface patterning techniques, investigated via in-house electromagnetic simulations. The proposed methods rely on the fabrication of an array-like structure at the VCSEL outcoupling facet, featuring just one unique super-mode distributed along the rectangular structure.

As a preliminary step, Section II reports a comparison between measured and simulated far-field (FF) data for a relief-based rectangular VCSEL, also accounting for thermal lensing phenomena. From this comparison, it is possible to derive an indirect measurement of the active region self-heating temperature. Then, in Section III, two different single mode designs are investigated, focusing on different strategies to achieve threshold reduction, injection uniformity and polarization control. Finally, Section IV deals with the non-axial FF profile that is typical of rectangular VCSELs (see [18] and Fig. 1), problematic for fiber coupling applications.

Valerio Torrelli, Alberto Tibaldi, Francesco Bertazzi, and Michele Goano are with the Department of Electronics and Telecommunications, Politecnico di Torino, 10129 Turin, Italy, and also with the Consiglio Nazionale delle Ricerche (CNR), Istituto di Elettronica e di Ingegneria dell'Informazione e delle Telecomunicazioni (IEIIT), 10129 Turin, Italy.

Alberto Gullino and Pierluigi Debernardi are with the Consiglio Nazionale delle Ricerche (CNR), Istituto di Elettronica e di Ingegneria dell'Informazione e delle Telecomunicazioni (IEIIT), 10129 Turin, Italy (e-mail: pierluigi.debernardi@polito.it).

## II. ELECTROMAGNETIC SOLVER APPLIED TO RECTANGULAR VCSELS: MODEL AND VALIDATION

Though the target emission wavelength is 795 nm, simulations are first applied to a standard wavelength of 850 nm, for which trial samples have been fabricated and experimental data are available.
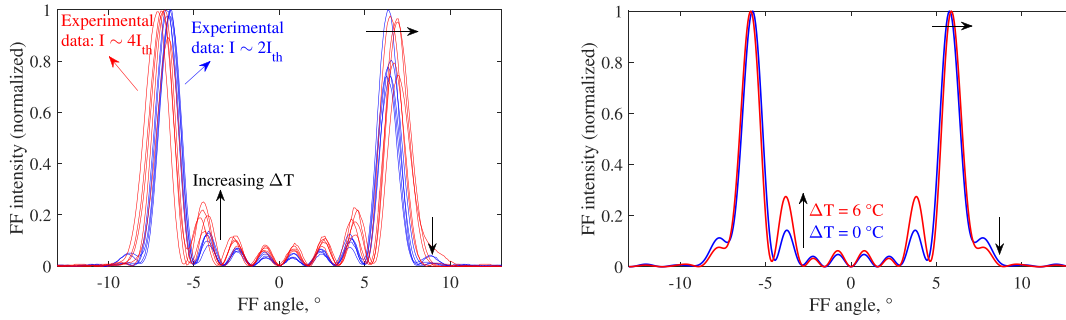
Fig. 1.    Left: horizontal cuts of the FF data for an 850 nm AlGaAs VCSEL with a patterned grating relief array at the outcoupling facet. Multiple curves of the same color refer to nominally equal devices in different positions of the wafer, while blue and red curves differ in terms of injection current, set at twice and four times the threshold current, respectively. Right: VELMS simulations of the same structure with a peak self-heating temperature $\Delta T$ of 0 and 6 °C. They provide the best fit with the experimental results after a parametric variation of $\Delta T$.

The scope of this section is to present the electromagnetic solver and its validation versus experimental FF data of a rectangular VCSELs emitting at 850 nm with an active area of $30 \times 4 \, \mu\mathrm{m}^2$ (aspect ratio of 7.5), whose outcoupling facet is patterned with a grating relief array of 8 elements. This is done to increase the single mode operation (a further discussion on this solution is reported in Section III).

This structure is investigated by means of our in-house Vcsel ELectroMagnetic suite (VELMS), first published in 2001 [20], used and validated against a variety of VCSEL designs [15], [19], [21], [22], [23], [24], [25], [26], [27], [28], also self-consistently coupled to carrier transport and thermal models for a comprehensive analysis of circular geometries [1], [29], [30], [31], [32], [33].

Following [20], the VCSEL is described as a stack of layers (thicknesses and refractive indices) perpendicular to the growth direction $z$. The fundamental input for the method is the epi-structure of the VCSEL, featuring thicknesses and material compositions. For the specific case of AlGaAs VCSELs, the composition is defined by the aluminum content, which is then translated into refractive index at the desired wavelength [34]. The method is based on the mode expansion technique. Indeed, the transverse component of the unknown field $\mathbf{E}_t$, depending on both $z$ and the transverse position $\boldsymbol{\rho}$, is expanded in terms of the basis formed by the transverse components of the cylindrical waves $\{\mathbf{e}_\mu\}$ ($\mu$ being a multi-dimensional label) of a uniform reference medium, i.e.,

$$\mathbf{E}_t\left(\boldsymbol{\rho}, z\right) = \sum_\mu a_\mu(z)\mathbf{e}_\mu(\boldsymbol{\rho}), \tag{1}$$

$\{a_\mu\}$ being the unknown expansion coefficients. At this point, these can be properly ordered and stored into an unknown vector $\underline{A}$, whose dimensions depend on the number of cylindrical waves used to represent the fields. From coupled mode theory [20], [23], it is known that, within a single layer, the $z$-dependency of $\underline{A}$ is governed by the coupled mode equations

$$\frac{d\underline{A}}{dz} = \left(\underline{\underline{\mathcal{B}}} + \underline{\underline{\mathcal{K}}}\right)\underline{A}, \tag{2}$$

$\underline{\underline{\mathcal{B}}}$ being a $\lambda$-dependent diagonal propagation matrix and $\underline{\underline{\mathcal{K}}}$ being the coupling matrix. Besides the formulas presented in [20], the

key message is that the $(\mu, \nu)$-entries of $\underline{\underline{\mathcal{K}}}$ can be obtained as a $\lambda$-dependent double integral over the transverse plane, involving the transverse profile of refractive index of the layer and the spatial distributions of the expansion and test cylindrical waves indexed by $\mu$ and $\nu$. For layers without transverse variations, the double integral can be calculated analytically by exploiting the orthonormality properties of the basis functions. On the other hand, for layers featuring a transverse variation of refractive index (such as the oxide layer), the overlap integrals provide the coupling terms of $\underline{\underline{\mathcal{K}}}$. For sake of efficiency, using polar coordinates and properly parameterizing the oxide shape, it is possible to perform the angular part of the double integral analytically, leaving just the radial integral to be performed numerically.

From (2), the generalized transmission matrix $\underline{\underline{M}}$ of a single layer of thickness $L$ can be found as

$$\underline{\underline{M}} = \mathrm{e}^{\left(\underline{\underline{\mathcal{B}}}+\underline{\underline{\mathcal{K}}}\right)L}, \tag{3}$$

from which the transmission matrix of a stack of layers simply becomes the product of the single-layer transmission matrices. Then, it is possible to determine the resonant condition exploiting the reflection matrices at the top and at the bottom of the resonator. To do that, one must also account for the modification of the refractive index of the active layer $\Delta n_\mathrm{a}$ induced by the gain. Finally, it is possible to obtain a $\lambda$-dependent eigenvalue equation for the vector of expansion coefficients, whose eigenvalues are proportional to $\Delta n_\mathrm{a}$. The emission frequency of the VCSEL transverse modes is obtained by searching numerically the zero of the real part of said eigenvalues, and the corresponding imaginary part provides the threshold gain.

The model is validated for its application on such rectangular structures against experimental FF data at different currents. To obtain a better match with experimental data, the thermal lensing phenomenon, i.e., the temperature-induced modification of the refractive index due to self-heating, has to be taken into account. To this end, a numerical solution of the heat equation was found using a simplified thermal source uniformly distributed within the rectangular active region. The obtained temperature profile features elliptical contour lines in the transverse plane. After translating the spatially-dependent temperature increase into a

refractive index variation in all of the VCSEL layers as done in [1], VELMS can be applied to the structure under analysis with a varying peak temperature rise $\Delta T$ with respect to the reference room temperature. This allows us to investigate how the FF profile varies with the self-heating temperature, increasing with the driving current.

Horizontal cuts (along the long side of the rectangle) of the experimental FF data are reported in Fig. 1 (left). The blue curves represent the FF patterns for nominally equal devices at the lowest injection current investigated, i.e., twice the threshold current of the device. On the other hand, the red curves represent the corresponding patterns for nominally equal devices at four times the threshold current, yielding a higher temperature. The FF profile is dominated by the two main side lobes, lacking a relevant radiated power in the axial direction. Increasing current (and self-heating), it is possible to notice a broadening of the FF aperture, a lowering of the side external lobes, and an increase of the strength of the internal peaks, more evident for the two lobes closest to the two main peaks (the trends with increasing self-heating are highlighted by black arrows). VELMS simulations for a peak self-heating temperature varying in $\{0, 6\}$ °C are reported in Fig. 1 (right), which provide the best fit with the experimental data. Besides finding a good agreement, also the trends are reproduced. From the simulations, one can grasp how much the temperature impacts on the various lobes, highlighting that the ones closest to the main two peaks are the most sensitive with temperature increase. Assuming a negligible self-heating at twice the threshold current, reasonable for devices like the ones investigated in [1], noticing that at four times the threshold the investigated sensitive peaks are doubled in relative intensity, one can infer that this corresponds to a peak self-heating temperature in the active region of about 6 °C.

## III. INVESTIGATED SINGLE-MODE DESIGNS

In this section, optimization strategies are applied to the target case-study of a rectangular VCSEL emitting at 795 nm. A lower aspect ratio, compared to that of the geometries investigated in Section II, is chosen to improve the readability of the devices. Yet, the optimization strategies presented in this section are absolutely general and could be applied to whatever geometry. The reason we are interested in elongated rectangles is to enhance the electrical injection uniformity in the active region and to mitigate the self-heating [18]. Indeed, in the case of a large-area squared VCSELs, the current density must undergo a longer path to reach the central active area than in a rectangle. Furthermore, a rectangle can dissipate the heat more efficiently on its shorter side, improving the thermal roll-over and single mode features [22].

More in detail, the investigated epi-structure is based on the 850-design, where the thicknesses have been downscaled to reach the target of 795 nm. The only difference lies in the QW AlGaAs composition, whose gain peak has to meet the target wavelength.

Compared to standard circular geometries, the oxide aperture is here a stretched rectangle with footprint $26 \times 6$ $\mu m^2$, i.e.,
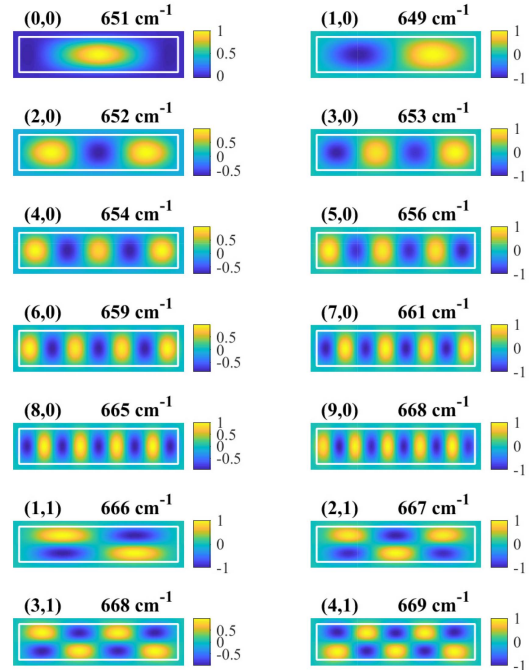


Fig. 2. Calculated mode profiles at the outcoupling facet of a rectangular VCSEL with their corresponding threshold gain. Only $x$-polarization is displayed; $y$-polarization features exactly the same threshold gain, wavelength and field profile, since in the simulation no intrinsic anisotropy is included. Each mode is indexed by the number of nodes along $x$ and $y$. Emission wavelengths are closely packed: all the modes in the figure lie within a wavelength interval of 0.5 nm.

more than 20 that of a typical circular single-mode device, hence yielding a much higher optical power.

Fig. 2 presents the modes, simulated with VELMS, of this device. These results agree qualitatively with [18]. Each mode is indexed by a two dimensional label of integer numbers, $(n_x, n_y)$, $n_x$ and $n_y$ being the number of nodes along $x$ and $y$, respectively. VELMS is a fully vectorial method, therefore each mode features the three components along $x$, $y$ and $z$. In Fig. 2 we are reporting the normalized dominant component of the modes at the outcoupling facet of the laser, namely the near-field profiles, together with their threshold gains. Since mode discrimination solutions are not applied here, they have similar threshold gains, which is compatible with the expected multi-mode emission.

Now, we present design strategies aimed at single-mode operation based on selecting a high-order mode by introducing threshold gain penalties for all its competitors. The fundamental idea is to introduce a patterning at the VCSEL aperture, which mimics the topography of the mode. Such patterning can be designed on the basis of the preliminary simulations presented in Fig. 2.

We discard the idea of selecting the modes with $n_y > 0$. Indeed, with such an aspect ratio, the patterned structures needed to select a mode with $n_y > 0$ should be quite small and thus more challenging from the manufacturing standpoint. The situation would be different for squared geometries like the one investigated in [22], for which modes with $n_x = n_y$ become a reasonable choice.
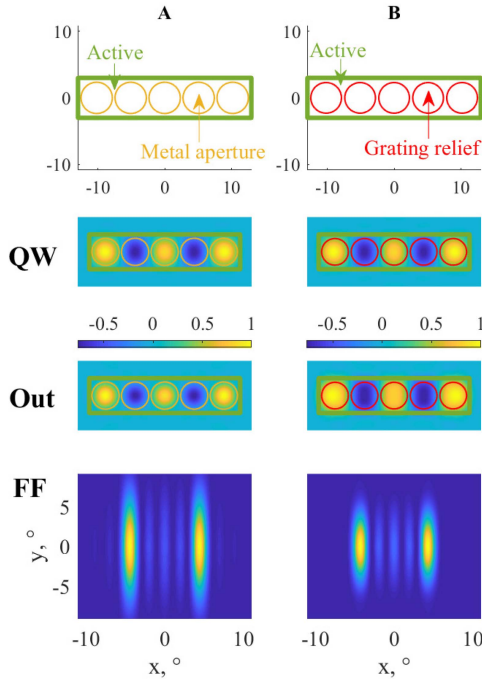
Fig. 3. Overview of the investigated designs (A and B) achieving the single-mode emission. Each column represents one of the designs, described in terms of transverse geometry (first row, axes are expressed in $\mu$m), dominant component of the mode with the lowest threshold at the QW section (second row), at the output section, i.e., the near field profile (third row), and far field profile. More in detail, design A features the oxide aperture sketched by the green line and is covered with metal everywhere except for the metal opening depicted in yellow. Design B instead features circular grating surface reliefs within the red circles.

TABLE I
PARAMETERS CHARACTERIZING DESIGNS A AND B

| design | $G_0^x$, cm$^{-1}$ | $G_0^y$, cm$^{-1}$ | $G_1$, cm$^{-1}$ | $\eta_o$ |
|---|---|---|---|---|
| A | 884 | 879 | 1080 | 0.55 |
| B | 1192 | 1634 | 1536 | 0.94 |

Among the modes with $n_y = 0$, considering that the aspect ratio of the rectangle is about 4, the mode (4,0) is the one featuring the most circular field spots, while the others are quite elliptical (see the limit cases with $n_x = 0$ and $n_x = 9$ featuring the highest ellipticity). For this reason, the target of the designs will be achieving single-mode, single-polarization (*e.g.*, $x$) operation with the (4,0) mode. The following subsections will present different possibilities to achieve this target.

The single-mode solutions investigated in this section rely on a metallic grid and a grating relief array at the VCSEL outcoupling facet, respectively, presented in Fig. 3. In view of a comparative appraisal between the design strategies, four parameters are investigated, which are summarized in Table I. These are:

- the threshold gain of the selected mode for both polarizations, $G_0^x$, and its $y$-polarized counterpart $G_0^y$,
- the threshold gain of the first superior (in gain) mode $G_1$,
- the outcoupling efficiency $\eta_o$, defined as the ratio of the optical power emitted by the device to that generated in the QW active region.

The various design strategies will be described in detail in the following subsections.

## Design A: metallic grid

The first investigated solution to retrieve the single-mode emission (design A), similarly to that simulated, realized and characterized in [22], is based on patterning the outcoupling facet with a metallic grid, consisting of a 50 nm Pt layer featuring 5 uniformly spaced apertures in correspondence to the field spots of the mode (4,0). For the design A, the first column of Fig. 3 shows the transverse features of the investigated geometry, the dominant component of the mode with the lowest threshold both at the QW section and at the outcoupling facet (near field), and the FF profile. The parameters characterizing the design are reported in the first row of Table I.

Design A features a relative difference between $G_0^y$ and $G_1$ of 23.4%, therefore much higher than the situation depicted in Fig. 2, where the maximum relative threshold difference between the modes is around 3%. Besides the optical advantages, this solution can also improve dramatically the electrical injection and its uniformity in the QWs, especially useful for very large apertures.

This design lacks any polarization control (nearly equal $G_0^x$ and $G_0^y$) and features a strong metal absorption (low outcoupling efficiency). If polarization control is not an issue, then efficiency can be improved by using elliptical metal apertures and this design can be used.

## Design B: grating relief array

The second investigated solution (design B) consists of a grating relief array, where each grating relief is aligned with one of the field spots of the mode (4,0). Similarly to the corresponding solution for circular VCSELs, the reflectivity of the $p$-DBR depends strongly on the thickness of the outcoupling layer, i.e., the cap layer. For a standard design, this thickness is optimized to have the maximum DBR reflectivity and the lowest threshold gain. In relief-based designs, the cap layer is grown longer, targeting the highest threshold gain, and subsequently etched, with a depth corresponding to the optimal design, following the transverse profile of the mode to be selected. This procedure strongly increases the thresholds for all the modes less than the selected one, hence acting as a mode selector. This design also allows for polarization control. Indeed, it is possible to etch a grating in the regions where the relief is needed.

In this work, a sub-wavelength grating is employed to reduce diffraction losses. More in detail, the grating alone is investigated with a rigorous coupled-waves analysis (RCWA) [26], [35], which estimates its reflection and transmission coefficients. These RCWA results are then identified with the reflection and transmission coefficients of an anisotropic layer, obtaining the ordinary and extraordinary refractive indexes of the corresponding uniaxial dielectric tensor [36], which can be included in VELMS. A sketch of the working principle is reported in Fig. 4.

From a quantitative standpoint, the thicknesses can be designed by computing the 1D threshold gain, i.e., by neglecting all transverse variations and focusing on the VCSEL stack for $\rho = 0$, as indicated with a vertical dashed line in Fig. 5. Aiming at maximizing the threshold gain *a priori* of the patterning, we choose a cap layer thickness of 90 nm. From there, the right
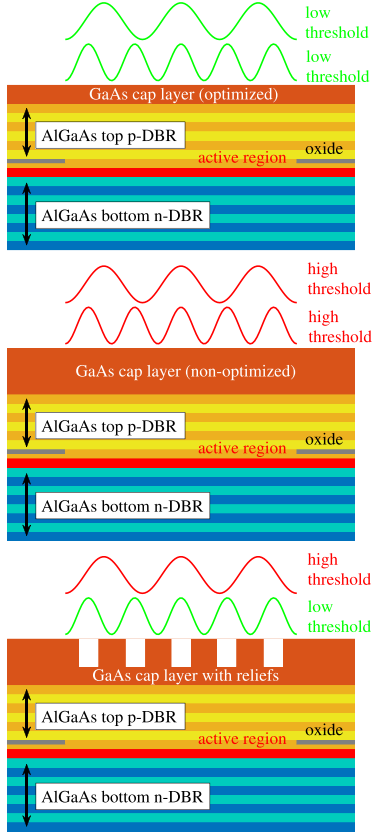
Fig. 4. Schematic of the relief design. For a standard VCSEL, the cap layer thickness is optimized to have the lowest threshold for all the modes such as (4,0) and (2,0), whose intensity is sketched above the laser (top). To only select the mode (4,0), it is possible to raise the cap layer thickness to a point where the threshold is high for all the modes (middle) and then etch in correspondence to the peaks of the mode (4,0) (bottom).
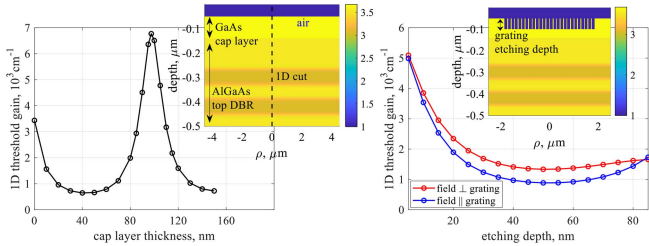


Fig. 5. Left: calculated threshold gain from 1D simulations as a function of the cap layer thickness. The inset represents the refractive index map of the structure, highlighting the 1D cut. Right: calculated threshold gain for the fields parallel and orthogonal to the grating bars with a fixed value of cap layer thickness of 90 nm. The inset shows the investigated sub-wavelength grating.

image shows how the threshold gain decreases as we etch into the cap layer, favoring the field parallel to the grating bars. We selected a grating etching depth of 50 nm, yielding the lowest threshold for the parallel field. Now, the full three-dimensional simulation can be carried out using the transverse geometry reported in the second column of Fig. 3. The parameters of this design are reported in the second row of Table I.

This geometry performs well as mode selector, yielding a satisfactory relative difference between $G_0^x$ and $G_1$ of 29.9% and an excellent control on the selected polarization given the high

value of $G_0^y$. Furthermore, the absence of metal at the output facet improves the outcoupling efficiency significantly with respect to design A, raising it as high as 0.94. The only downside of such a design is the higher threshold even for the wanted mode (4,0), due to the reduced DBR reflectivity introduced by the portions of non-optimized cap layer and by the absence of metal (note that a metallic layer, besides introducing optical losses, increases the overall reflectivity of the DBR, reducing the threshold).

## IV. OPTIMIZATION OF FF PATTERN FOR FIBER COUPLING

A possible disadvantage of both designs in Section III concerns their FF profile, in compliance with [18] and Fig. 1. Indeed, it presents two strong symmetric side lobes, leaving the central axial direction with little to no radiated power, significantly worsening the efficiency in the case of fiber coupling [9], [10], [37]. This is due to the alternating positive and negative peaks in the near field profile, resulting in a destructive interference effect. Looking at Fig. 2, it is possible to see that the positive and negative peak values are exactly symmetric for the modes with an odd $n_x$, while slightly asymmetric for the modes with an even $n_x$, for which the destructive interference is less significant. This leads the corresponding FF profile to show more radiated power in the axial direction, another valid reason to focus on selecting the mode (4,0) instead of the mode (3,0), which also presents pretty circular contour lines. In general, mitigating the destructive interference is a way to retrieve more power in central FF region, but from Fig. 3 we can see that choosing an even $n_x$ is not enough.

The solutions proposed in this section (designs C and D) aim at achieving the single-mode emission while simultaneously inhibiting the destructive interference effect resulting from the near field profile, overall retrieving a central peak in the FF.

### Design C: covered grating relief array

Design C combines designs A and B. Specifically, a grating relief array corresponding only to the three positive field spots of the mode (4,0) is used for mode selection and polarization discrimination, while a 50 nm thick Pt layer is deposited on top of the outcoupling facet. The latter features three rectangular apertures in correspondence to the positive field spots where the reliefs are localized, while simultaneously covering the negative field spots. The results are reported in the first column of Fig. 6. It can be noticed that, at the QW section, the field profile is exactly the expected profile of the mode (4,0), featuring both positive negative spots. However, at the output section, the near-field is strongly affected by the metallic cover layer, yielding a strong reduction of the negative field, whilst leaving the positive regions mostly unaffected. This heavily inhibits the destructive interference phenomena, yielding a FF profile with a central peak, much better for fiber coupling applications.

The figures of merit qualifying this design are summarized in the first row of Table II, showing a good relative separation between $G_0^x$ and $G_1$ of 22.2%, together with an excellent polarization control and an improved electrical injection with respect to design B thanks to the presence of the metal. Notice that the value of $G_0^x$ for the design C is lower with respect to the
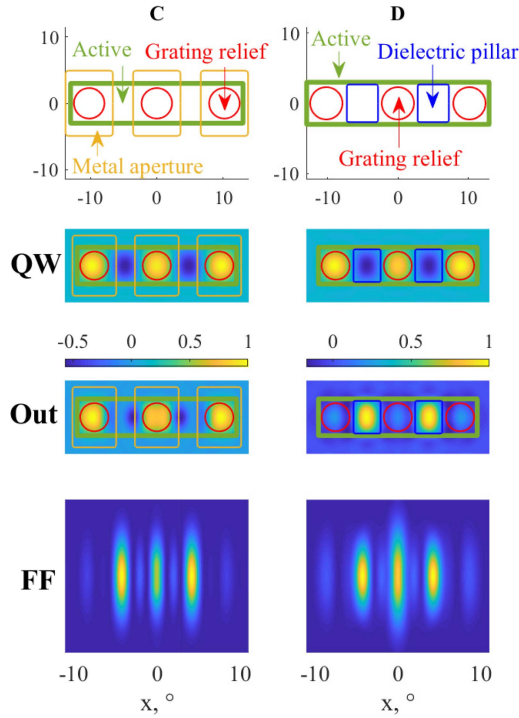
Fig. 6. Overview of the investigated designs (C and D) achieving the single-mode emission and optimizing the FF pattern, retrieving a central peak along the axial direction. The designs are described in the same terms as the ones in Fig. 3. Specifically, design C combines grating surface reliefs (indicated red circles) with metal apertures (indicated with yellow rectangles). Design D instead combines grating surface reliefs (withing red circles) with square dielectric pillars indicated in blue.

TABLE II
PARAMETERS CHARACTERIZING DESIGNS C AND D

| design | $G_0^x$, cm$^{-1}$ | $G_0^y$, cm$^{-1}$ | $G_1$, cm$^{-1}$ | $\eta_o$ |
|--------|------|------|------|------|
| C | 1145 | 1944 | 1399 | 0.65 |
| D | 1314 | 2363 | 1735 | 0.92 |

corresponding value for the design B, once again confirming that the metal layer is able to reduce the VCSEL threshold gain due to the increased reflectivity. Of course, the outcoupling efficiency is worsened due to the increased optical losses.

To quantify the strength of the central FF peak, it is possible to introduce the FF ratio $R_{FF}$, defined as the ratio between the central FF peak to one of the two side peaks. One can imagine that a thicker metallic layer induces a stronger inhibition of the destructive interference, yielding a larger $R_{FF}$, a reduction of $G_0^x$ due to the added reflectivity and a reduction of $\eta_o$ due to the added losses. This is investigated in Fig. 7.

As expected, $G_0^x$ is a decreasing function of the metal thickness, with most of its variation taking place within the first 100 nm, $\eta_o$ is a decreasing function with a linear behavior after 50 nm and $R_{FF}$ shows an increasing behavior, saturating after 150 nm. A trade-off between $\eta_o$ and $R_{FF}$ is highlighted. One can notice that choosing a metal thickness of 50 nm already provides a FF ratio of 73%, with an outcoupling efficiency of 65%. Exceeding this value of metal thickness could lead to an excessive worsening of $\eta_o$, this however depends on the specific application.
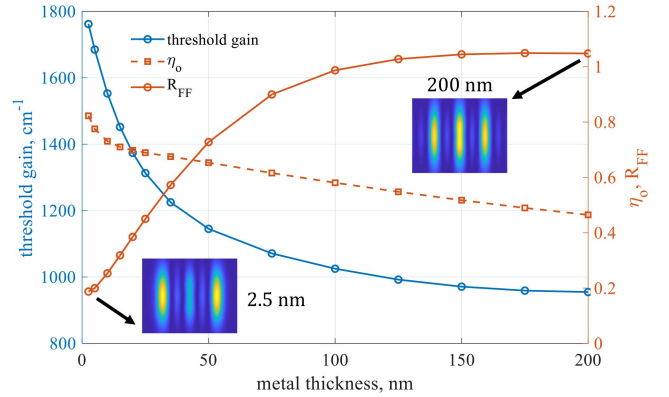


Fig. 7. Impact of the metal thickness on the threshold gain $G_0^x$, outcoupling efficiency $\eta_o$ and FF ratio $R_{FF}$ for the design C.

### Design D: grating relief array with dielectric pillars

Finally, the last investigated solution (design D) aims at achieving the central FF peak without worsening the outcoupling efficiency, at the cost of a higher threshold gain $G_0^x$. To achieve this, three grating reliefs in correspondence to the positive field spots are used for mode and polarization selection just like in design C. However, the negative field spots are not inhibited via a lossy metallic layer, but rephased by means of 100 nm thick $Si_3N_4$ pillars grown on top of the outcoupling facet in correspondence to the negative field spots. The results are reported in the last column of Fig. 3. Once again, it is possible to see the usual profile of the mode (4,0) at the QW section, which dramatically changes at the outcoupling facet. Indeed, the color bar displays an extreme reduction of the negative portion of the field, with the second and fourth near field peaks now being positive and dominant with respect to the others. This in turns reduces the destructive interference, yielding a strong central peak in the FF profile. The characteristics of this design are reported in the second row of Table II. It features a great relative difference between $G_0^x$ and $G_1$ of 32.0%, an excellent polarization control and an almost unaffected outcoupling efficiency with respect to design B. The downsides with respect to design C (linked to the absence of a metallic layer) are a worsened electrical injection and a relevant increase of $G_0^x$ of 14.8%, translating into a higher threshold current. If the fiber-coupling application under investigation only requires a high efficiency and a good coupling, giving up the lowest possible threshold current, this represents a better solution with respect to design C.

## V. CONCLUSION

In this work, we applied our in-house electromagnetic solver VELMS to relief-based large-area rectangular VCSELs. The excellent agreement with the experimental results further validates our code and allow us to infer an estimation of the peak self-heating temperature in the active region from the deformation of FF profiles with respect to the cold-cavity case. We applied VELMS to predict the impact of different design strategies, looking for optimized solutions to achieve single-mode emission within the context of large-area VCSELs for high-power atomic excitation. We investigated four designs, based on selecting a

high-order mode via the patterning of the outcoupling facet of the resonator. For applications for which a good electrical injection and a low threshold is needed, not requiring polarization control, design A can be used. On the other hand, if the device threshold is not an issue, design B can be employed, also ensuring the polarization discrimination via the etching of a sub-wavelength grating. Finally, for fiber coupling applications requiring an axial FF pattern, both designs C and D can be used. Design C is particularly useful for threshold reduction and electrical injection, while design D can be employed for maintaining a high outcoupling efficiency.

All of these techniques can be scaled for different aspect ratios and different sizes and can be combined to achieve different effects, depending on the specific applications.

## REFERENCES

[1] A. Tibaldi, F. Bertazzi, M. Goano, R. Michalzik, and P. Debernardi, "VENUS: A vertical-cavity surface-emitting laser electro-opto-thermal NUmerical simulator," *IEEE J. Select. Topics Quantum Electron.*, vol. 25, no. 6, Nov./Dec. 2019, Art. no. 1500212.

[2] G. K. Veerabathran, S. Sprengel, A. Andrejew, and M.-C. Amann, "Room-temperature vertical-cavity surface-emitting lasers at 4 $\mu$m with GaSb-based type-II quantum wells," *Appl. Phys. Lett.*, vol. 110, 2017, Art. no. 071104.

[3] G. Pan, M. Xun, Z. Zhao, Y. Sun, J. Zhou, and D. Wu, "High slope efficiency bipolar cascade 905nm vertical cavity surface emitting laser," *IEEE Electron Device Lett.*, vol. 42, no. 9, pp. 1342–1345, Sep. 2021.

[4] M. Huang, D. K. Serkland, and J. Camparo, "A narrow-linewidth three-mirror VCSEL for atomic devices," *Appl. Phys. Lett.*, vol. 121, no. 11, 2022, Art. no. 114002.

[5] M. Xun et al., "High single fundamental-mode output power from 795nm VCSELs with a long monolithic cavity," *IEEE Electron Device Lett.*, vol. 44, no. 7, pp. 1144–1147, Jul. 2023.

[6] Y. Zhou et al., "Large-aperture single-mode 795nm VCSEL for chip-scale nuclear magnetic resonance gyroscope with an output power of 4.1mW at 80°C," *Opt. Exp.*, vol. 30, no. 6, pp. 8991–8999, Mar. 2022.

[7] K. Jin et al., "Design of portable self-oscillating VCSEL-pumped cesium atomic magnetometer," *MDPI Electron.*, vol. 11, no. 22, Nov. 2022, Art. no. 3666.

[8] M. A. Bobrov et al., "Optically pumped non-zero field magnetometric sensor for the magnetoencephalographic systems using intra-cavity contacted VCSELs with rhomboidal oxide current aperture," *J. Phys. Conf. Ser.*, vol. 1697, 2020, Art. no. 012175.

[9] L. S. Watkins et al., "High power VCSEL devices for atomic clock applications," *Proc. SPIE*, vol. 9616, 2015, Art. no. 96160J.

[10] Q. Liu, Z. Chai, J. Lu, K. Yin, and J. Li, "Development of non-magnetic VCSEL module for compact atomic magnetometer," *Proc. SPIE*, vol. 12311, 2022, Art. no. 123110U.

[11] Y. Zhou et al., "Wavelength tuning robustness optimization for a high-temperature single-mode VCSEL used in chip-scale atomic sensing systems," *Appl. Opt.*, vol. 61, no. 9, pp. 2417–2423, Mar. 2022.

[12] N. A. Maleev, S. A. Blokhin, M. A. Bobrov, A. G. Kuz'menkov, M. M. Kulagina, and V. M. Ustinov, "Laser source for a compact nuclear magnetic resonance gyroscope," *Gyroscopy Navigation*, vol. 9, no. 3, pp. 177–182, 2018.

[13] L. Bai et al., "Quantum-enhanced rubidium atomic magnetometer based on Faraday rotation via 795nm Stokes operator squeezed light," *J. Opt.*, vol. 23, no. 8, Aug. 2021, Art. no. 085202.

[14] A. J. A. Carvalho, R. S. N. Moreira, J. Ferraz, S. S. Vianna, L. H. Acioli, and D. Felinto, "Enhanced absorption of weak ultrashort light pulses by a narrowband atomic medium," *Phys. Rev. A*, vol. 101, May 2020, Art. no. 053426.

[15] P. Debernardi, A. Kroner, F. Rinaldi, and R. Michalzik, "Surface relief versus standard VCSELs: A comparison between experimental and hot-cavity model results," *IEEE J. Sel. Topics Quantum Electron.*, vol. 15, no. 3, pp. 828–837, May/Jun. 2009.

[16] Å. Haglund, J. S. Gustavsson, J. Vukusic, P. Modh, and A. Larsson, "Single fundamental-mode output power exceeding 6mW from VCSELs with a shallow surface relief," *IEEE Photon. Technol. Lett.*, vol. 16, no. 2, pp. 368–370, Feb. 2004.

[17] S. Gronenborn et al., "High-power VCSELs with a rectangular aperture," *Appl. Phys. B*, vol. 105, pp. 783–792, 2011.

[18] S. Gronenborn, T. Schwarz, P. Pekarski, M. Miller, H. Mönch, and P. Loosen, "Optical modes in a rectangular VCSEL resonator with properties of both Gaussian and Fourier modes," *IEEE J. Quantum Electron.*, vol. 48, no. 8, pp. 1040–1044, Aug. 2012.

[19] V. Torrelli, A. Tibaldi, F. Bertazzi, M. Goano, and P. Debernardi, "Modeling of single-mode high-power VCSEL arrays," in *Proc. IEEE 23rd Int. Conf. Numer. Simul. Optoelectron. Devices*, 2023, pp. 93–94.

[20] G. P. Bava, P. Debernardi, and L. Fratta, "Three-dimensional model for vectorial fields in vertical-cavity surface-emitting lasers," *Phys. Rev. A*, vol. 63, no. 2, 2001, Art. no. 23816.

[21] P. Debernardi, G. P. Bava, C. Degen, I. Fischer, and W. Elsäßer, "Influence of anisotropies on transverse modes in oxide-confined VCSELs," *IEEE J. Quantum Electron.*, vol. 38, no. 1, pp. 73–84, Jan. 2002.

[22] P. Debernardi, G. P. Bava, F. Monti di Sopra, and M. B. Willemsen, "Features of vectorial modes in phase-coupled VCSEL arrays: Experiments and theory," *IEEE J. Quantum Electron.*, vol. 39, no. 1, pp. 109–119, Jan. 2003.

[23] P. Debernardi and G. P. Bava, "Coupled mode theory: A powerful tool for analyzing complex VCSELs and designing advanced devices features," *IEEE J. Select. Topics Quantum Electron.*, vol. 9, no. 3, pp. 905–917, May/Jun. 2003.

[24] P. Debernardi, J. M. Ostermann, M. Sondermann, T. Ackemann, G. P. Bava, and R. Michalzik, "Theoretical-experimental study of the vectorial modal properties of polarization-stable multimode grating VCSELs," *IEEE J. Sel. Topics Quantum Electron.*, vol. 13, no. 5, pp. 1340–1348, Sep./Oct. 2007.

[25] P. Debernardi, "HOT-VELM: A comprehensive and efficient code for fully vectorial and 3-D hot-cavity VCSEL simulation," *IEEE J. Quantum Electron.*, vol. 45, no. 8, pp. 979–992, Aug. 2009.

[26] A. Tibaldi, P. Debernardi, and R. Orta, "High-contrast grating performance issues in tunable VCSELs," *IEEE J. Quantum Electron.*, vol. 51, no. 12, Dec. 2015, Art. no. 2400407.

[27] R. Orta, A. Tibaldi, and P. Debernardi, "Bimodal resonance phenomena– Part I: Generalized Fabry–Pérot interferometers," *IEEE J. Quantum Electron.*, vol. 52, no. 12, Dec. 2016, Art. no. 610050.

[28] P. Debernardi et al., "Modal performance of spiral phase plate VCSELs," *IEEE J. Quantum Electron.*, vol. 52, no. 5, May 2016, Art. no. 2400108.

[29] P. Debernardi, A. Tibaldi, M. Daubenschüz, R. Michalzik, M. Goano, and F. Bertazzi, "Probing thermal effects in VCSELs by experiment-driven multiphysics modeling," *IEEE J. Sel. Topics Quantum Electron.*, vol. 25, no. 6, Nov./Dec. 2019, Art. no. 1700914.

[30] A. Tibaldi et al., "Bridging scales in multiphysics VCSEL modeling," *Opt. Quantum Electron.*, vol. 51, no. 7, Jul. 2019, Art. no. 231.

[31] A. Gullino et al., "Modulation response of VCSELs: A physics-based simulation approach," in *Proc. IEEE 20th Int. Conf. Numer. Simul. Optoelectron. Devices*, 2020, pp. 65–66.

[32] A. Gullino, A. Tibaldi, F. Bertazzi, M. Goano, and P. Debernardi, "Reduced dimensionality multiphysics model for efficient VCSEL optimization," *MDPI Appl. Sci.*, vol. 11, no. 15, 2021, Art. no. 6908.

[33] A. Gullino et al., "Physics-based modeling of AlGaAs tunnel junction VCSELs: A comparative appraisal," in *Proc. IEEE 23rd Int. Conf. Numer. Simul. Optoelectron. Devices*, 2023, pp. 99–100.

[34] M. A. Afromowitz, "Refractive index of Ga$_{1-x}$Al$_x$As," *Solid State Commun.*, vol. 15, pp. 59–63, Feb. 1974.

[35] P. Debernardi, R. Orta, T. Gründl, and M.-C. Amann, "3-D vectorial optical model for high-contrast grating vertical-cavity surface-emitting lasers," *IEEE J. Quantum Electron.*, vol. 49, no. 2, pp. 137–145, Feb. 2013.

[36] M. Born and E. Wolf, *Principles of Optics. Electromagnetic Theory of Propagation, Interference and Diffraction of Light*, 7th ed.Cambridge, U.K.: Cambridge Univ. Press, 1999.

[37] C. Johnson, P. D. D. Schwindt, and M. Weisend, "Magnetoencephalography with a two-color pump-probe, fiber-coupled atomic magnetometer," *Appl. Phys. Lett.*, vol. 97, no. 24, Dec. 2010, Art. no. 243703.